

# *Inverse identification of local stiffness across ascending thoracic aortic aneurysms*

**Solmaz Farzaneh, Olfa Trabelsi &  
Stéphane Avril**

**Biomechanics and Modeling in  
Mechanobiology**

ISSN 1617-7959

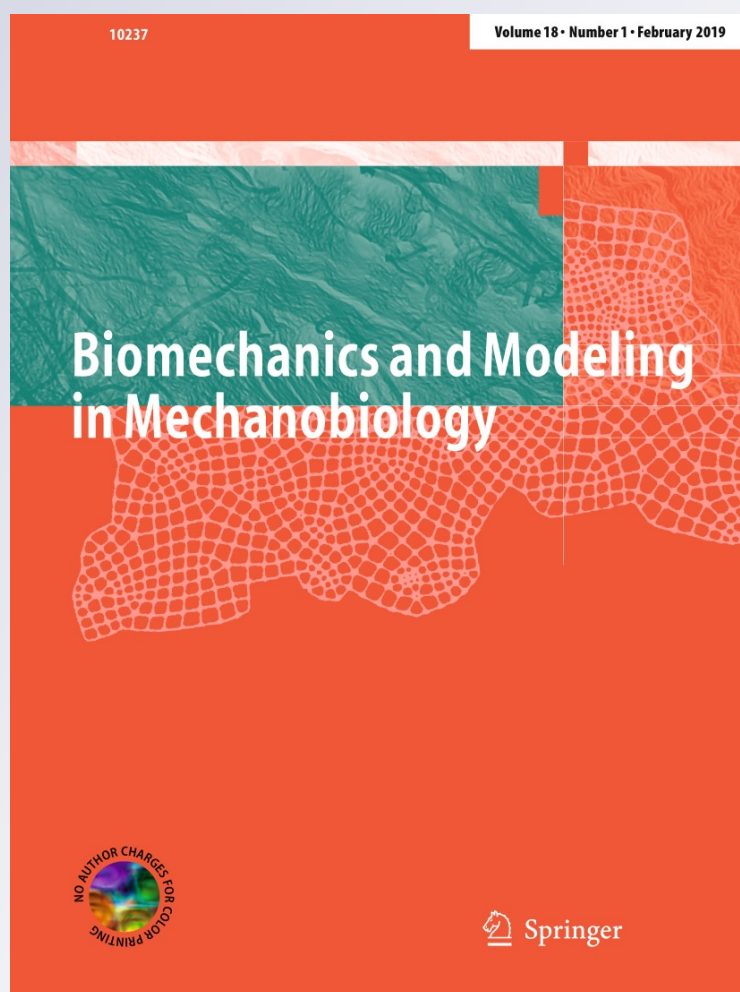
Volume 18

Number 1

Biomech Model Mechanobiol (2019)

18:137-153

DOI 10.1007/s10237-018-1073-0



**Your article is protected by copyright and all rights are held exclusively by Springer-Verlag GmbH Germany, part of Springer Nature. This e-offprint is for personal use only and shall not be self-archived in electronic repositories. If you wish to self-archive your article, please use the accepted manuscript version for posting on your own website. You may further deposit the accepted manuscript version in any repository, provided it is only made publicly available 12 months after official publication or later and provided acknowledgement is given to the original source of publication and a link is inserted to the published article on Springer's website. The link must be accompanied by the following text: "The final publication is available at [link.springer.com](http://link.springer.com)".**



# Inverse identification of local stiffness across ascending thoracic aortic aneurysms

Solmaz Farzaneh<sup>1,2,3</sup> · Olfa Trabelsi<sup>1,2,3</sup> · Stéphane Avril<sup>1,2,3</sup> Received: 2 March 2018 / Accepted: 16 August 2018 / Published online: 25 August 2018  
© Springer-Verlag GmbH Germany, part of Springer Nature 2018

## Abstract

Aortic dissection is the most common catastrophe of the thoracic aorta, with a very high rate of mortality. Type A dissection is often associated with an ascending thoracic aortic aneurysm (ATAA). However, it is widely acknowledged that the risk of type A dissection cannot be reliably predicted simply by measuring the ATAA diameter and there is a pressing need for more reliable risk predictors. It was previously shown that there is a significant correlation between a rupture criterion based on the ultimate stretch of the ATAA and the local extensional stiffness of the aorta. Therefore, reconstructing regional variations of the extensional stiffness across the aorta appears highly important. In this paper, we present a novel noninvasive inverse method to identify the patient-specific local extensional stiffness of aortic walls based on preoperative gated CT scans. Using these scans, a structural mesh is defined across the aorta with a set of nodes attached to the same material points at different time steps throughout the cardiac cycle. For each node, time variations of the position are analyzed using Fourier series, permitting the reconstruction of the local strain distribution (fundamental term). Relating these strains to tensions with the extensional stiffness, and writing the local equilibrium satisfied by the tensions, the local extensional stiffness is finally derived at every position. The methodology is applied onto the ascending and descending aorta of three patients. Interestingly, the regional distribution of identified stiffness properties appears heterogeneous across the ATAA. Averagely, the identified stiffness is also compared with values obtained using other nonlocal methodologies. The results support the possible noninvasive prediction of stretch-based rupture criteria in clinical practice using local stiffness reconstruction.

**Keywords** Noninvasive inverse method · Local extensional stiffness · Finite-elements · Ascending thoracic aortic aneurysms · Patient-specific · Risk of rupture

## 1 Introduction

Ascending thoracic aortic aneurysms (ATAAs) manifest by localized ballooning of the aorta. They are difficult to detect because they usually have no symptom. Unrecognized and untreated TAA may lead to dissection or rupture of the aneurysm ending with instantaneous death. Independently of age and gender, about 30,000 people in Europe and 15,000

people in the United States are diagnosed with a TAA every year (Bickerstaff et al. 1982; Johansson et al. 1995; Ramanath et al. 2009).

ATAAs are commonly treated with a timely surgical repair by replacement of the dilated aortic segment with synthetic grafts. For patients without any familial disorders such as Marfan syndrome, elective surgical intervention of ATAA is recommended when its diameter is larger than 5.5 cm or when it is considered as a fast-growing aneurysms (growth > 1 cm per year) (Chau and Elefteriades 2013; Coady et al. 1999, 1997; Elefteriades and Farkas 2010; Johansson et al. 1995). The diameter of 5.5 cm as a criterion for decision-making of surgical intervention is extensively recognized as an insufficient criterion. For example, the International Registry of Acute Aortic Dissection (IRAD) conveyed that among 591 type “A” aortic dissections, 59% had a diameter below 5.5 cm. Moreover, several studies considering abdominal aortic aneurysms (AAA) suggest that biomechanical factors may

**Electronic supplementary material** The online version of this article (<https://doi.org/10.1007/s10237-018-1073-0>) contains supplementary material, which is available to authorized users.

✉ Stéphane Avril  
avril@emse.fr

<sup>1</sup> Mines Saint-Étienne, CIS-EMSE, 42023 Saint-Étienne, France

<sup>2</sup> INSERM, U1059, SAINBIOSE, 42023 Saint-Étienne, France

<sup>3</sup> Université de Lyon, 69000 Lyon, France

reliably predict the risk of rupture rather than the diameter criterion alone (Fillinger et al. 2003; Geest et al. 1085; McGloughlin 2011). Wall stress analysis and identification of patient-specific material properties of abdominal aortic aneurysms using 4D ultrasound were performed to improve rupture risk assessment (Disseldorp et al. 2016). It is well-known that the rupture of ATAA occurs when the stress applied to the aortic wall reaches the rupture stress (Malvindi et al. 2016; Martufi et al. 2014; Trabelsi et al. 2015). Another definition of rupture can be represented when the stretch applied to the tissue is greater than its maximum extensibility or distensibility (stretch-based rupture criterion). Accordingly, Duprey et al. (2016) proposed a stretch-based rupture risk criterion and showed its correlation with tangent elastic modulus in ATAA based on data collected in 31 patients. In that study, individual rupture stretch and tangent elastic moduli were determined *in vitro* by means of bulge inflation tests on the identical ATAA wall tissue segments that had been excised intraoperatively. Trabelsi et al. (2017) proposed a method for the *in vivo* identification of the (global) stiffness of an aortic segment based on the determination of volumetric distensibility from gated CT scans and pulsed pressure. However, only moderate correlation was found between the global *in vivo* stiffness values and the (local) stretch-based rupture risk criterion determined from bulge inflation tests on excised tissue segments of 13 ATAA. Therefore, the assessment of the local elastic properties of the ATAA wall from *in vivo* data that are clinically available might be a crucial point for establishing a reliable method of estimation of ATAA rupture risk (Mousavi et al. 2017). In the present paper, a new inverse approach to this task is presented.

This is meaningful as stiffening of the aortic wall is both a cause and a consequence of ATAA (Choudhury et al. 2009; Vorp et al. 2003). Stiffening leads to a decrease of extensibility due to loss of elastin and deposition of collagen during growth and remodeling. There are studies that have indeed demonstrated such stiffening (without wall weakening) in age-matched subjects (Iliopoulos et al. 2009; García-Herrera et al. 2008). They mostly found local variations of mechanical parameters along the longitudinal direction, indicating higher strength and peak elastic modulus along the circumferential direction compared to the longitudinal direction (Iliopoulos et al. 2009). Therefore, identifying noninvasively the *in vivo* elastic properties of the aorta would help clinicians to take decisions whether the patient needs surgical intervention. Besides, the mechanical properties can be used to perform computational analyses, the accuracy of which will rely on the accuracy of input parameters.

However, noninvasive characterization of elastic properties is not the most common approach for deriving material properties of aortas. The most common methods to obtain material properties are *in vitro* uniaxial and biaxial mechanical tests (Choudhury et al. 2009; Geest et al. 2004; Okamoto

et al. 2002). They permit plotting stress–strain curves and deriving parameters of strain energy functions or linearized elastic moduli of the aneurysmal walls at different stages of loading (Vorp et al. 2003). Several studies have characterized the mechanical properties of ATAA via strain energy functions and elastic moduli indicating that ATAA causes stiffening and extensibility reduction. To assess rupture risk on a patient-specific level, their results imply decreased tissue compliance as a rupture risk factor (Sokolis et al. 2012; Martin et al. 2013).

To our best knowledge, no study has ever identified regional variations of material properties in ATAAs on a patient-specific basis using a noninvasive methodology. Therefore, the main objective of this work is to present a novel methodology based on gated CT images for the identification of local stiffness properties in ATAAs under assumptions of linearized and isotropic elasticity. After a comprehensive presentation, we present different numerical validations of the methodology and show exemplary results on three patients for the proof of concept.

## 2 Material and methods

### 2.1 Origin of data

After informed consent and according to a protocol approved by the Institutional Review Board of the University Hospital Center of Saint-Etienne, noninvasive systolic and diastolic blood pressures in brachial artery and gated CT scans were obtained for three patients who underwent elective surgical repair of ATAA at the University Hospital of Saint-Etienne (CHU-SE) in France. The demographic information of these patients is recorded in Table 1. For each patient, images were recorded at ten phases of their cardiac cycle. These images were used to reconstruct the geometry of their whole aorta, including diastolic and systolic phases. Semi-automatic segmentation of the CT image slices was done using MIMICS (v.10.01, Materialise NV). The three-dimensional (3D) surface of the aorta was generated for each phase and exported as STL format. All phases were cut by the same cross-sectional planes to predefine a domain of the aorta larger than the final segment of interest in both ascending and descending parts. The purpose was to initiate the procedure in order to run the Vascular Modeling Toolkit (VMTK, Orobix, Bergamo, Italy; [www.vmtk.org](http://www.vmtk.org)) (Antiga and Steinman 2004) and to derive the parametric coordinates of the surface. The same smoothing factor was applied at all phases. To recognize the systolic and diastolic phases, the luminal volumes of all phases were compared. The systolic scan was defined as the one with the largest volume and the diastolic scan as the one with the smallest volume. See Fig. 1 in which each phase is shown using a different color.

**Table 1** Demographic information of three patients

Patient ID	Sex	Age	$\Delta P$ (KPa) (mmHg)	$Q_{in-vivo}$ (MPa mm)	$Q_{in-vitro}$ (MPa mm)
1	M	27	8.66 (65)	1.96	0.78
2	M	84	13.4 (100.5)	6.14	4.11
3	M	61	11.5 (86)	4.6	1.24

Note that  $\Delta P$  is the difference between diastolic and systolic pressures,  $Q_{in-vivo}$  denotes the extensional stiffness obtained by Trabelsi et al. (2017) and  $Q_{in-vitro}$  is the extensional stiffness obtained by Duprey et al. (2016)

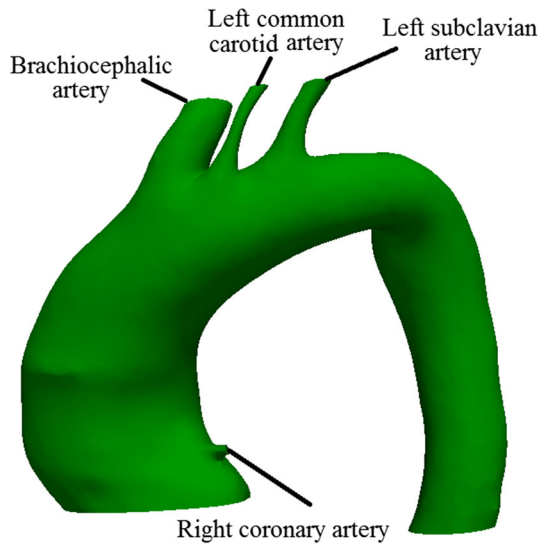


**Fig. 1** Segmentation of the aortic geometry for diastolic phase. Including left subclavian artery, brachiocephalic artery, left common carotid artery and coronary artery branches which are used as anatomical references. See video 1 in supplemental materials to visualize the ten phases of the whole cardiac cycle

### 2.2 Theory of the inverse approach

A set of nodes was defined across each reconstructed aortic geometry, with the requirement that a node represented the position of the same material point at each phase of the cardiac cycle. For this, it was essential to reconstruct a structural mesh for all phases with an identical number of elements and nodes and to have a mesh morphing function between the geometries of each phase.

VMTK (Antiga and Steinman 2004) was employed to generate the structural mesh from STL files. The method was based on centerlines and decomposition of the surface into existing branches and mapping each branch onto template parametric coordinates. Once a bifurcation is split into branches, each branch is topologically equivalent to a cylinder and can be mapped onto a set of rectangular parametric coordinates (Antiga and Steinman 2004). The approach for mapping the surface of bifurcations consisted of several steps: calculation of centerlines, definition of the reference system, decomposition of the bifurcation into its branches and their parameterization. VMTK provides a technique

based on objective criteria capable of generating consistent parameterizations over a wide range of bifurcating geometries. Let  $\partial\Omega_i$  be the surface of the  $i$ th branch which is delimited by two topological circles  $\psi_{i0}$  and  $\psi_{iL}$ . Considering  $u \in [0, L_i]$  is the longitudinal parametric coordinate and  $v \in [-\pi, \pi]$  is the periodic circumferential parametric coordinate, over the parametric space of  $U \subset \mathbb{R}^2$  in the coordinates  $U = (u, v)$ , a bijective mapping is derived as (Antiga and Steinman 2004)

$$\Phi : \partial\Omega_i \rightarrow U \tag{1}$$

such that  $\Phi(\mathbf{x}) = (0, v)$  on  $\psi_{i0}$  and  $\Phi(\mathbf{x}) = (L_i, v)$  on  $\psi_{iL}$ . Longitudinal mapping in VMTK is created by a harmonic and a stretch function to achieve localization with respect to centerline abscissa and reference system (Haker et al. 2000). The harmonic function  $f = f(\mathbf{x})$  with  $\mathbf{x} \in \partial\Omega_i$  is computed by solving the elliptic partial differential equation as

$$\Delta_B f = 0 \tag{2}$$

where  $\Delta_B$  is the Laplace–Beltrami operator. The longitudinal parametric coordinate is expressed by

$$u(\mathbf{x}) = s \circ f(\mathbf{x}) \tag{3}$$

where  $s$  is the stretch function and can be defined as

$$s(f) = \frac{1}{|\lambda(f)|} \int_{\lambda(f)} g(\mathbf{x}) d\lambda \tag{4}$$

where  $\lambda(f)$  indicates a level-set of  $f$ . The angular position of each node is determined by a set of normals along the curve of frame  $\tau$ , named  $\mathbf{n}(\tau)$  (which is directed toward the center of the osculating circle of the curve at each point), and its nearest point on the centerline,  $\mathbf{c}(\tau)$ , as

$$v(\mathbf{x}) = \arccos((\mathbf{x} - \mathbf{c}(\tau)) \cdot \mathbf{n}(\tau)) \tag{5}$$

where  $\tau$  indicates the different time frames.

One of the requirements is that the inlets and outlets of the imported mesh into VMTK should be open. Left subclavian artery, brachiocephalic artery, left common carotid artery and coronary artery branches were used to provide anatomical

references to ensure that the measurements taken at different phases of the cardiac cycle were at the same location in the aorta (see Fig. 1). Eventually, the extracted data from VMTK were postprocessed in MATLAB to extract an accurate mesh using the longitudinal and circumferential metrics obtained from VMTK. A template meshgrid with an arbitrary number of points was created in the  $u_{temp} \in [u_{min}, u_{max}]$  and  $v_{temp} \in [-\pi, \pi]$  domain. A polynomial approximation was implemented around each node of the template meshgrid. For instance, let  $(u_{temp}^i, v_{temp}^i)$  denote the parametric coordinates of node  $\mathbf{X}_i$ . Let  $(\mathbf{u}_{nb}, \mathbf{v}_{nb})$  be the parametric coordinates of the nodes of the reconstructed STL surface around  $\mathbf{X}_i$ . These nodes were selected such that  $du_j = (u_{nb}^j - u_{temp}^i) < \delta_u$  and  $dv_j = (v_{nb}^j - v_{temp}^i) < \delta_v$ ,  $\delta_u$  and  $\delta_v$  defining the size of the neighborhood. We assumed  $\delta_u = 8$  mm and  $\delta_v = \pi/5$  rad. Therefore using the least-squares method, the polynomial approximation was written such as

$$\mathbf{A}\mathbf{X} = \mathbf{X}_{nb} \tag{6}$$

with

$$\mathbf{A} = \begin{bmatrix} 1 & du_1 & dv_1 & du_1dv_1 & du_1^2 & dv_1^2 & du_1^2dv_1 & du_1dv_1^2 \\ \vdots & \vdots \\ 1 & du_k & dv_k & du_kdv_k & du_k^2 & dv_k^2 & du_k^2dv_k & du_kdv_k^2 \\ \vdots & \vdots \\ 1 & du_n & dv_n & du_ndv_n & du_n^2 & dv_n^2 & du_n^2dv_n & du_ndv_n^2 \end{bmatrix} \tag{7}$$

$$\mathbf{X} = \begin{bmatrix} X_1 & Y_1 & Z_1 \\ X_2 & Y_2 & Z_2 \\ \vdots & \vdots & \vdots \\ X_8 & Y_8 & Z_8 \end{bmatrix} \tag{8}$$

and

$$\mathbf{X}_{nb} = \begin{bmatrix} X_{nb}^1 & Y_{nb}^1 & Z_{nb}^1 \\ \vdots & \vdots & \vdots \\ X_{nb}^k & Y_{nb}^k & Z_{nb}^k \\ \vdots & \vdots & \vdots \\ X_{nb}^n & Y_{nb}^n & Z_{nb}^n \end{bmatrix} \tag{9}$$

Based on a mesh sensitivity analysis, an average mesh size of  $1 \times 1$  mm was used. According to Wittek et al. (2016) who observed that the ascending thoracic aorta experiences clockwise and counterclockwise twist, we derived the time variations of the circumferential coordinate,  $v$ , of coronary arteries in the space of parametric coordinate and subtracted this value from the circumferential coordinate of the assumed reference phase in order to apply torsion during aortic wall motion. To adjust all phases longitudinally, the origin of  $u$  was set in the coronary plane at each phase. Accordingly, the torsion was applied by subtracting the shift of the  $v$  value at the inlet, and by subtracting a shift in the  $v$  value all along

the thoracic aorta, varying linearly from  $v$  to 0 between the inlet and the position of the brachiocephalic artery.

Any periodic function [in this case nodal coordinates of all phases,  $x(t)$ ] can be expressed as a weighted sum of infinite series of sine and cosine functions of varying frequency. Therefore, having the structural mesh of all ten phases, a discrete Fourier transform was employed such as

$$x(t) = a_0 + \sum_{n=1}^{\infty} (a_n \cos(nft) + b_n \sin(nft)) \tag{10}$$

Where  $a_0$  is the direct current (DC) term and the sum is the fundamental magnitude of the time-varying node positions when  $n=1$  while  $f$  is the fundamental frequency. A strain analysis was performed on the average geometry (defined by using the DC terms of all nodal positions) by applying displacements (including torsion) at each node corresponding to the fundamental term obtained from the Fourier transform in Eq. 10. As the fundamental term is complex, the real and the imaginary parts are applied separately at the corresponding nodes (in their average position, defined by the DC term) using the finite element method (FEM). Eventually, the reconstructed strain components were also complex. The components in the longitudinal and circumferential directions were derived respectively as

$$\begin{aligned} \varepsilon_1^{com} &= \varepsilon_1^r + i\varepsilon_1^{im} \\ \varepsilon_2^{com} &= \varepsilon_2^r + i\varepsilon_2^{im} \end{aligned} \tag{11}$$

where superscripts ‘‘r’’ and ‘‘im’’ indicate real and imaginary contributions, respectively. Therefore the magnitude of strains in the longitudinal and circumferential directions can be respectively obtained as

$$\begin{aligned} \varepsilon_1 &= \sqrt{\varepsilon_1^{r2} + \varepsilon_1^{im2}} \\ \varepsilon_2 &= \sqrt{\varepsilon_2^{r2} + \varepsilon_2^{im2}} \end{aligned} \tag{12}$$

The results of the strain computation are independent of the chosen material properties and this methodology is applicable to finite deformation problems. Although the aortic tissue is globally anisotropic and nonlinear, we linearized here its mechanical behavior in the range of strains induced by pressure variations between diastole and systole, and neglected anisotropic effects in this range too. The constitutive equations reduced to Hooke’s law in plane stress. Due to the spatial resolution of CT, the local aortic thickness cannot be measured accurately in vivo. The thickness was previously measured in vitro on the excised sample after the surgery (Duprey et al. 2016). However, the in vitro measurement is performed when the tissue is load free, whereas the tissue is stretched and pressurized in vivo. Therefore the thickness

can vary significantly in vivo, thus to express the Hooke's law, we wrote the membrane tensions,  $\tau$ , as

$$\begin{aligned} \tau_1(t) &= \tau_1^0 + Q(\varepsilon_1(t) + \nu\varepsilon_2(t)) \\ \tau_2(t) &= \tau_2^0 + Q(\nu\varepsilon_1(t) + \varepsilon_2(t)) \end{aligned} \tag{13}$$

where  $\tau_1^0$  and  $\tau_2^0$  are the DC terms of both components of the membrane tension (representing pretensions existing in the average geometry due to average blood pressure and axial tension),  $Q$  is the extensional stiffness and  $\nu$  is the Poisson's ratio in which incompressibility is assumed ( $\nu = 0.49$ ). We derived  $\tau_1^0$  and  $\tau_2^0$  by achieving an FE stress analysis on the average geometry under the effect of the average pressure  $P_0$  using the approach proposed by Joldes et al. (2016).

As shown in Fig. 2 it is assumed that each element of the arterial wall is a finite sector of an ellipsoidal membrane with radii  $r_1$  and  $r_2$  in both circumferential and longitudinal directions. So, in the framework of these assumptions, local equilibrium equations can be written as

$$P(t) = \frac{\tau_1(t)}{r_1(t)} + \frac{\tau_2(t)}{r_2(t)} \tag{14}$$

where  $r_1$  and  $r_2$  are the radii of the element sector in both directions (major and minor) as shown in Fig. 2 and  $P$  is the applied pressure. Using  $P_0$  to denote the DC term of pressure variations, and neglecting second order variations, Eq. 14 is rewritten:

$$\begin{aligned} P(t) - P_0 &= \frac{\tau_1(t) - \tau_1^0}{r_1^0} \\ &+ \frac{\tau_2(t) - \tau_2^0}{r_2^0} - \frac{\tau_1^0(r_1(t) - r_1^0)}{(r_1^0)^2} - \frac{\tau_2^0(r_2(t) - r_2^0)}{(r_2^0)^2} \end{aligned} \tag{15}$$

Using  $\Delta P$ ,  $\Delta\tau_1$ ,  $\Delta\tau_2$ ,  $\Delta r_1$  and  $\Delta r_2$  to denote the fundamentals of pressure, the circumferential and longitudinal components of the local tension tensor, and the circumferential and longitudinal radius of curvature, respectively, Eq. 15 is written as follows:

$$\Delta P = \frac{\Delta\tau_1}{r_1^0} + \frac{\Delta\tau_2}{r_2^0} - \frac{\tau_1^0(\Delta r_1)}{(r_1^0)^2} - \frac{\tau_2^0(\Delta r_2)}{(r_2^0)^2} \tag{16}$$

In the following, we assume  $\Delta P = (P_{\text{sys}} - P_{\text{dias}})/2$ .

Substituting Eqs. 13 in 16, we obtain the extensional stiffness for each element such as

$$Q = \frac{\Delta P + \frac{\tau_1^0 \Delta r_1}{(r_1^0)^2} + \frac{\tau_2^0 \Delta r_2}{(r_2^0)^2}}{\frac{\varepsilon_1(t) + \nu\varepsilon_2(t)}{r_1^0} + \frac{\nu\varepsilon_1(t) + \varepsilon_2(t)}{r_2^0}} \tag{17}$$

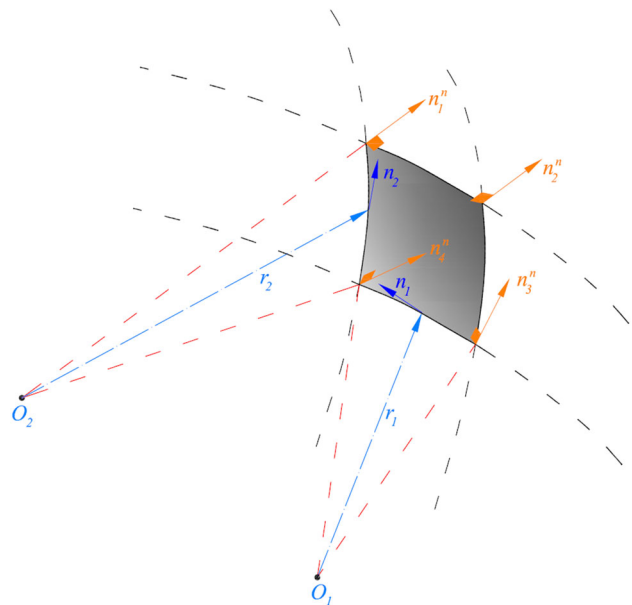


**Fig. 2** It is assumed that each element of the arterial wall is a finite sector of an ellipsoidal membrane with radii  $r_1$  and  $r_2$  in both circumferential and longitudinal directions.  $n_1$  and  $n_2$  are tangential unit vectors normal to  $r_1$  and  $r_2$ , respectively.  $n_i^n$  with  $i = \{1, 2, \dots, 4\}$  is normal unit vector at each node of the element

To obtain  $r_1$  and  $r_2$  fast and efficiently, we developed a method based on the principle of virtual work as previously introduced in Bersi et al. (2016), so assuming stresses  $\sigma$  at equilibrium with external loads  $\mathbf{T}$  should satisfy the following equation:

$$\int_v \sigma_{ij} : \varepsilon_{ij}^* dv + \int_{\partial v} T_i u_i^* ds = 0 \tag{18}$$

where  $v$  is the volume of the domain of interest,  $\partial v$  is its surface boundary,  $\mathbf{u}^*$  is a virtual continuous displacement field and  $\varepsilon^*$  are the virtual strains related to the gradients of the virtual displacements. As this equation is valid for any virtual field,  $\mathbf{u}^*$  can be defined as a unit vector oriented along the normal directions of the aortic wall at every node (directions  $n_{1,2,3,4}^n$  in Fig. 2) to inflate virtually the aorta. Accordingly, it is possible to derive the following local equation:

$$\sigma_1 h \varepsilon_1^* + \sigma_2 h \varepsilon_2^* = pu^* \tag{19}$$

where  $\sigma_1$  and  $\sigma_2$  are the principal components of the stress and  $h$  is the thickness. The Laplace law may be written:

$$\frac{\sigma_1}{r_1} h + \frac{\sigma_2}{r_2} h = p \tag{20}$$

By identification between the two previous equations, we obtain directly a relationship between the local radii of cur-

vature and the virtual strain fields:

$$\begin{aligned}\frac{1}{r_1} &= \frac{\varepsilon_1^*}{u^*} \\ \frac{1}{r_2} &= \frac{\varepsilon_2^*}{u^*}\end{aligned}\quad (21)$$

In the current study we used the concept of “extensional stiffness” which equals the material stiffness times the thickness and whose dimension is MPa mm.

Stiffness variations across the different regions of the thoracic aorta may exist at different scales. In order to filter out high-frequency variations, the obtained results were eventually fitted using Fourier polynomial of order 4 along the circumferential directions and polynomials of order 3 along the axial direction, permitting a smoother estimation of stiffness distribution.

### 2.3 Numerical implementation

We reconstructed ascending and descending aortas excluding all branches. Therefore, the right coronary and brachiocephalic arteries were used as reference points to obtain identical parts of the ascending aorta at different phases and the left subclavian artery was used as a reference point to consider identical parts of the descending aorta at different phases. For each patient and each phase, a structural mesh using quadrilateral elements with four nodes was prepared and then the average structural meshes of ascending and descending aortas were obtained by averaging the nodal positions throughout the cardiac cycle. Afterward, for each aorta, the Abaqus FE software (Hibbitt, Karlsson & Sorensen 2011) was employed to calculate  $\varepsilon_1^*$  and  $\varepsilon_2^*$  by applying  $u^*$  at each node in normal directions of  $n_1^n:n_4^n$  in Fig. 2. Moreover, two other independent FE analyses were performed by applying corresponding real and imaginary displacements at each node (including aorta torsion) to calculate  $\varepsilon_1^{\text{com}}$  and  $\varepsilon_2^{\text{com}}$  and subsequently  $\varepsilon_1$  and  $\varepsilon_2$  expressed in Eq. 12. For each FE analysis, orientation user subroutine (ORIENT) was employed to assign local material directions in order to save results in the local coordinate system. Each geometry was a nonperfectly cylindrical geometry so that the radial direction (normal to the artery) was defined as the outward normal direction to each element, the axial direction was defined as the direction parallel to the luminal centerline in the direction of the blood flow, and the circumferential direction was perpendicular to both previously defined directions. To calculate and visualize the local extensional stiffness expressed in Eq. 17, a user material subroutine (UMAT) and a user-defined external databases (UEXTERNALDB) were coupled with the commercial FE software Abaqus (Hibbitt, Karlsson & Sorensen 2011). The complete methodology is summarized in a flowchart shown in Fig. 3.

In summary, we had to perform several different steps to characterize the local aortic stiffness for each patient. The most time-consuming step was the segmentation of CT images (cleaning could last 1 day for the noisiest). Generation of the structural mesh took about 10 min including VMTK and further processing. It took less than 2 h to prepare the ABAQUS input files for stress analyses, strain analyses, stiffness assessment and reconstruction. Each ABAQUS resolution took about 5 min.

## 3 Results

### 3.1 Numerical validation

Numerical validation was performed considering two different material behaviors: linear isotropic elasticity and nonlinear anisotropic hyperelasticity.

### 3.2 Linear elastic material property

For the sake of validation, we used a reference aortic geometry (RG) and we created numerically a deformed aortic geometry (DG) by considering the effects of an average intramural pressure [ $P = 40$  mmHg (5.33 KPa)] onto the aorta modeled with a linear elastic behavior. The DG was derived by a finite element analysis using the raw STL mesh of the reference geometry. Two analyses (cases) were performed: one with a homogeneous stiffness in the whole aorta and another one with a heterogeneous stiffness distribution in which three regions were defined in the aorta, each one with a different stiffness as shown in Fig. 6. Each analysis provided a deformed STL mesh. Displacement maps used to reconstruct DG are shown in Fig. 4. Having in hand RG and DG for both cases, we performed our approach using VMTK and MATLAB to independently generate the structural mesh of each geometry. For the sake of validation, we subtracted the nodal coordinates of both structural meshes (on RG and DG). As it can be observed in Fig. 5, we found a good agreement between the displacements reconstructed using our approach and the reference displacement, indicating that structural meshes of both geometries are related to nearly similar material points. After this first validation on the reconstructed displacement data, we applied the whole methodology with reconstruction of stiffness distributions from the two simulated cases. For each case, a stiffness distribution was obtained and compared to the reference one (Fig. 6). The reconstructed stiffness was in good agreement with the reference and especially the local heterogeneity could be well retrieved for the heterogeneous case. Artifacts only appear very locally at the proximal and distal parts of the aortic segment due to spurious effects of polynomial smoothing close to the boundary (edge effects).

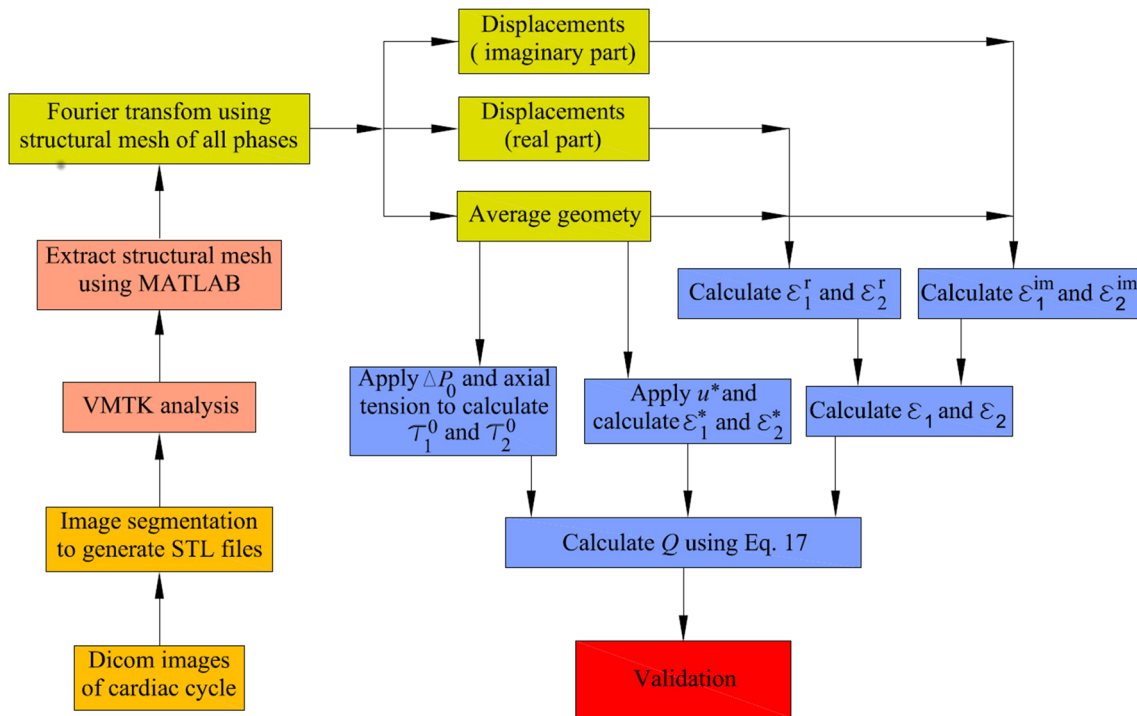


Fig. 3 Flowchart of the methodology to identify local extensional stiffness of aorta.  $\Delta P_0$  is average blood pressure

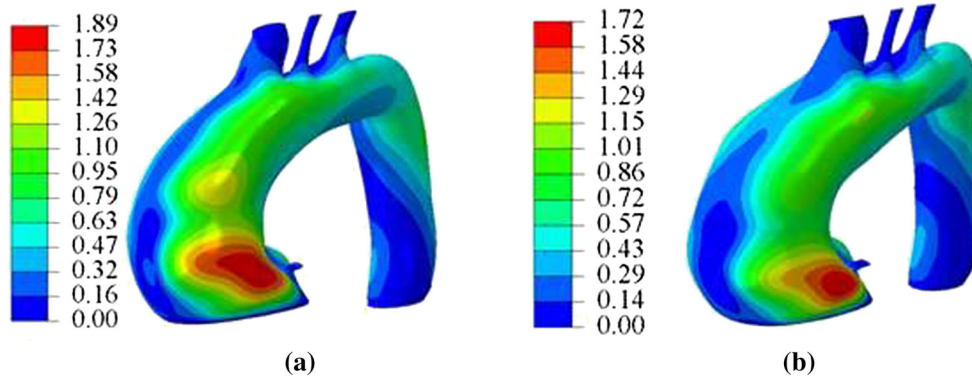


Fig. 4 Map of the displacement magnitude (mm) after inflation of the reference geometry (RG) using FE analysis considering **a** a homogenous stiffness and **b** a heterogeneous stiffness distributions

### 3.3 Nonlinear anisotropic material property

We have performed a complementary validation of our methodology considering anisotropy and effects of nonlinearity. We used the same aortic geometry (raw stl) as the one used for the linearized case study, which is the aortic geometry of a real patient which was segmented from a CT scan obtained at  $P_{diastole} = 80$  mmHg (10.66 KPa). We modeled the aortic wall with a Gasser–Ogden–Holzapfel anisotropic strain energy function which may be written as (Holzapfel et al. 2000a)

$$\bar{\Psi} = C_{10}(\bar{I}_1 - 3) + \frac{k_1}{2k_2} \sum_{i=4,6} \left[ \exp[k_2(\bar{I}_i - 1)^2] - 1 \right] + \kappa(J - 1)^2 \tag{22}$$

where  $C_{10}$  and  $k_1$  are material parameters and have a stress-like dimension, and  $k_2$  is a dimensionless material parameters while  $\kappa$  is the bulk modulus and  $J$  is the Jacobian.  $\bar{I}_1 = tr(\bar{C})$ ,  $\bar{I}_4 = \bar{C} : a_{01} \otimes a_{01}$  and  $\bar{I}_6 = \bar{C} : a_{02} \otimes a_{02}$  are respectively the first, fourth and sixth invariant of the modified counterparts of the right Cauchy–Green tensor,  $\bar{C}$ . Note that the two families of collagen fibers are character-

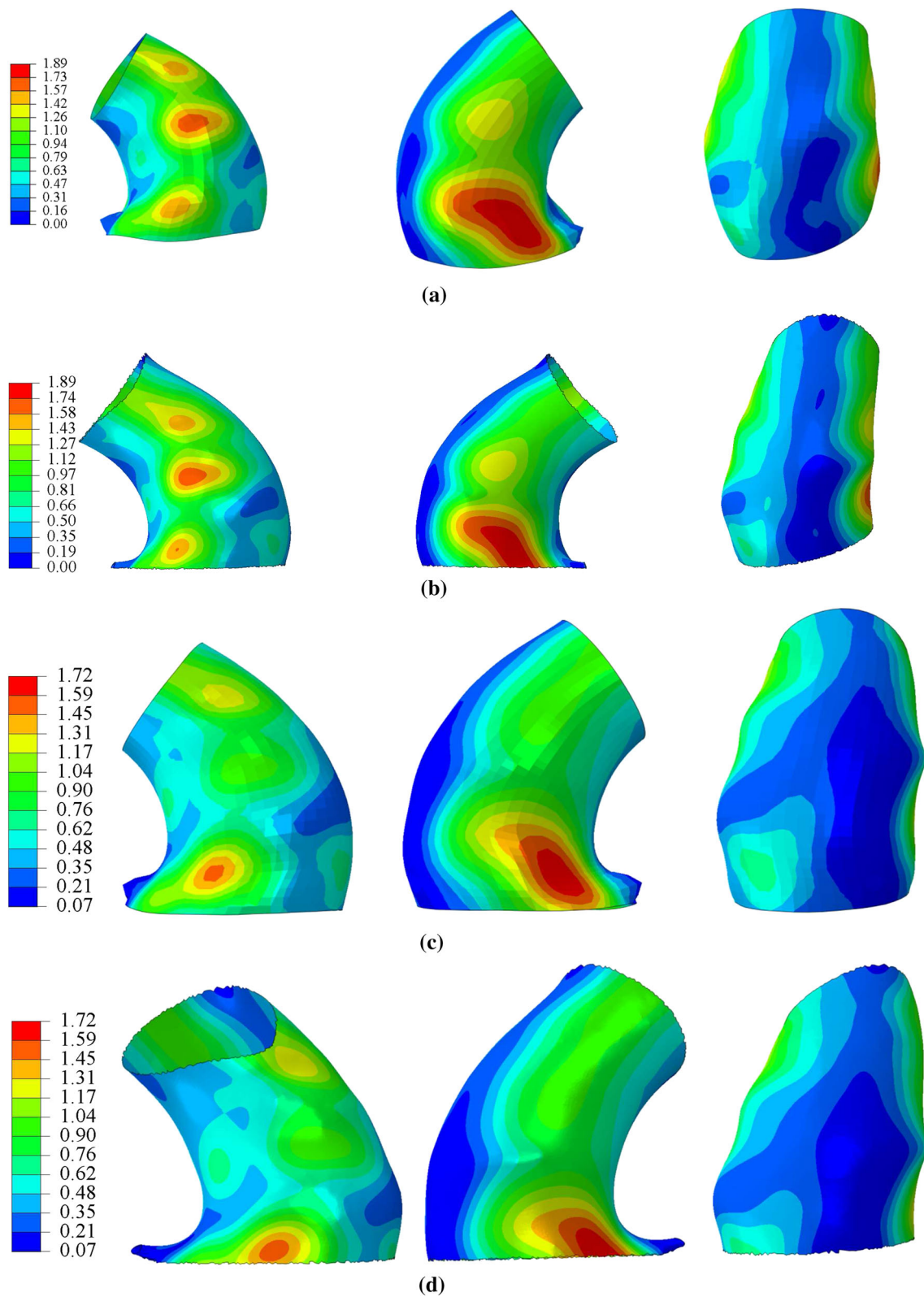
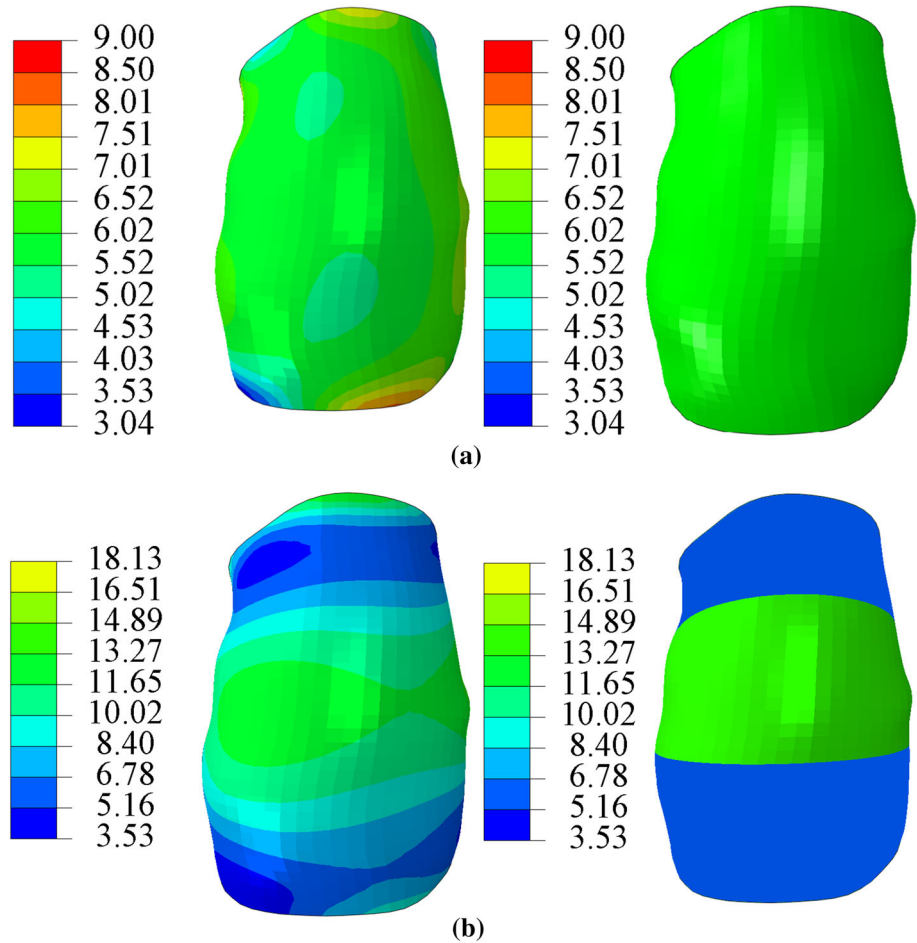


**Fig. 5** **a** Displacement maps (mm) obtained by our methodology considering a homogenous stiffness, **b** reference displacement maps obtained using a finite element analysis considering a homogenous stiffness, **c** displacement maps obtained by our methodology considering

a heterogeneous stiffness distribution, **d** reference displacement maps obtained using a finite element analysis considering a heterogeneous stiffness distribution

**Fig. 6** Validation study: stiffness map (MPa mm) reconstructed using our methodology (left) for the assigned homogeneous stiffness (right) (a). Stiffness map reconstructed using our methodology (left) for the assigned heterogeneous stiffness (right) (b)



ized by two orientation vectors  $a_{01} = [0 \cos\theta \sin\theta]$  and  $a_{02} = [0 \cos\theta -\sin\theta]$ , where  $\theta$  is the orientation angle.

Two analyses were performed: One with a homogeneous distribution of hyperelastic material properties in the whole ascending thoracic aorta and the other with a heterogeneous distribution of hyperelastic material properties, considering three regions. Material parameters used for this validation study are reported in Table 2. Before applying these two models to calculate displacements between diastole and systole, we first computed the zero pressure geometry in each case using the approach presented by Mousavi and Avril (2017), Mousavi et al. (2017). Afterward, we calculated the deformation of the aortic geometry for a systolic pressure directly by applying  $P_{\text{systole}} = 120 \text{ mmHg}$  (16 kPa) onto the zero pressure geometry.

Having in hand the diastolic geometry and the computed systolic geometry, we applied our approach using VMTK and MATLAB to independently generate the structural mesh of each geometry (systolic and diastolic) in both homogeneous and heterogeneous analyses. We subtracted the nodal coordinates of both structural meshes (systolic and diastolic phases) to obtain the displacements between systole and diastole for

each case. Assuming the diastolic phase as the reference geometry we applied our methodology to retrieve the local aortic stiffness properties. The identified results shown in Fig. 7 demonstrate that our methodology is able to retrieve the “stiff” region in the heterogeneous case, whereas the homogeneous case shows only small variations which are mostly related to edge effects. However, this remains a qualitative comparison as the obtained linearized stiffness is not directly related to hyperelastic properties. This qualitative validation completes well the previous quantitative validation where we modeled the aorta with a linear elastic behavior and where we were able to retrieve the correct stiffness properties.

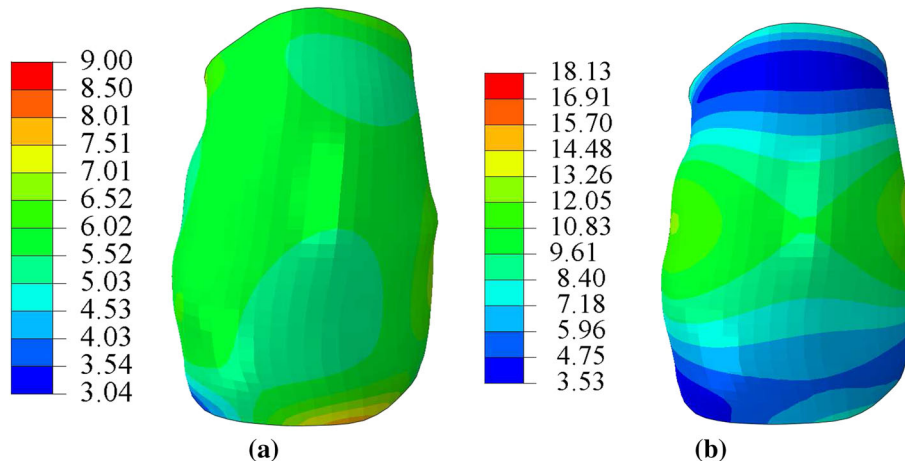
### 3.4 Patient-specific results

The methodology described previously was applied on 3 patients. The extensional stiffness of their aorta was reconstructed at every Gauss point of the mesh (excluding the branches and the region of the arch between the brachiocephalic and the left subclavian arteries) and then the values were interpolated at nodal positions. The results were plotted as independent colormaps which are shown in Fig. 8. The

**Table 2** Values of nonlinear anisotropic material parameters for homogeneous and heterogeneous models

	$C_{10}$ (kPa mm)	$k_1$ (kPa mm)	$k_2$	$\theta_1$ (°)	$\theta_2$ (°)
Homogenous	30	500	5	35	- 35
Heterogeneous stiff	60	1000	5	35	- 35
Heterogeneous compliant	30	500	5	35	- 35

**Fig. 7** Validation study: stiffness map (MPa mm) reconstructed using our methodology considering **a** homogeneous and **b** heterogeneous hyperelastic anisotropic material properties



distributions appear heterogeneous, especially in the ATAA regions where some regions of relatively higher extensional stiffness appear. The distribution of local extensional stiffness showed higher values for ascending aortas compared to descending aortas.

### 3.5 Comparison of the results

For these 3 patients, elastic properties of their ATAA were previously characterized with two other methods:

1. An ATAA segment was defined by two transverse planes located respectively at 10 cm and 55 cm from the coronary artery. Across the defined segment, the average distensibility of the ascending thoracic aorta was assessed from CT scans according to Trabelsi et al. (2017)

$$D_V = \frac{\Delta V}{V \Delta P} \tag{23}$$

where  $V$ ,  $\Delta V$  and  $\Delta P$  are respectively the luminal volume, the volume difference between diastole and systole and the pressure difference. The extensional stiffness was deduced as the ratio between the distensibility and the average diameter of the segment. Let  $Q_{in-vivo}$  denote the extensional stiffness obtained with this method.

2. After the surgical intervention on these patients, an ATAA segment was excised. From this segment, a square (45 × 45 mm) was cut in the outer curvature region and tested in bulge inflation. The stress–strain response of

the tested sample was linearized over a range of pressures inducing similar tensions in the tissue as the tensions produced by diastolic and systolic pressures. The obtained linearized stiffness of the tissue over this range, multiplied by tissue thickness, yielded another estimate of the extensional stiffness, which was denoted  $Q_{in-vitro}$ .

Therefore, for each patient, we focused on the distribution of extensional stiffness across the ATAA segment and across the cut square (Fig. 9). For the sake of statistical analysis, we derived the median and interquartile ranges of all nodal values of the identified extensional stiffness (Fig. 10). The analysis was achieved first by taking all the values of the ascending aorta, then only the values in the ATAA segment and finally only the values of the cut square. For each patient, we also plotted in Fig. 10 the  $Q_{in-vitro}$  and  $Q_{in-vivo}$  values obtained by Duprey et al. (2016) and Trabelsi et al. (2017), respectively. This analysis showed that the median and interquartile values for different cuts of all patients are relatively at the same ranges. Comparing the interquartile box obtained in this study with the corresponding results of Trabelsi et al. (2017), it can be deduced that for all patients  $Q_{in-vivo}$  is a value between the lower and the median value (mostly close to median) while  $Q_{in-vitro}$  values are close to lower corresponding interquartile. This can be explained by the mechanical actions of surrounding tissues and environment in vivo, which may apply a counter pressure on the artery. We did not take into account this counter pressure in the identification as  $P(t)$  in Eq. 14.

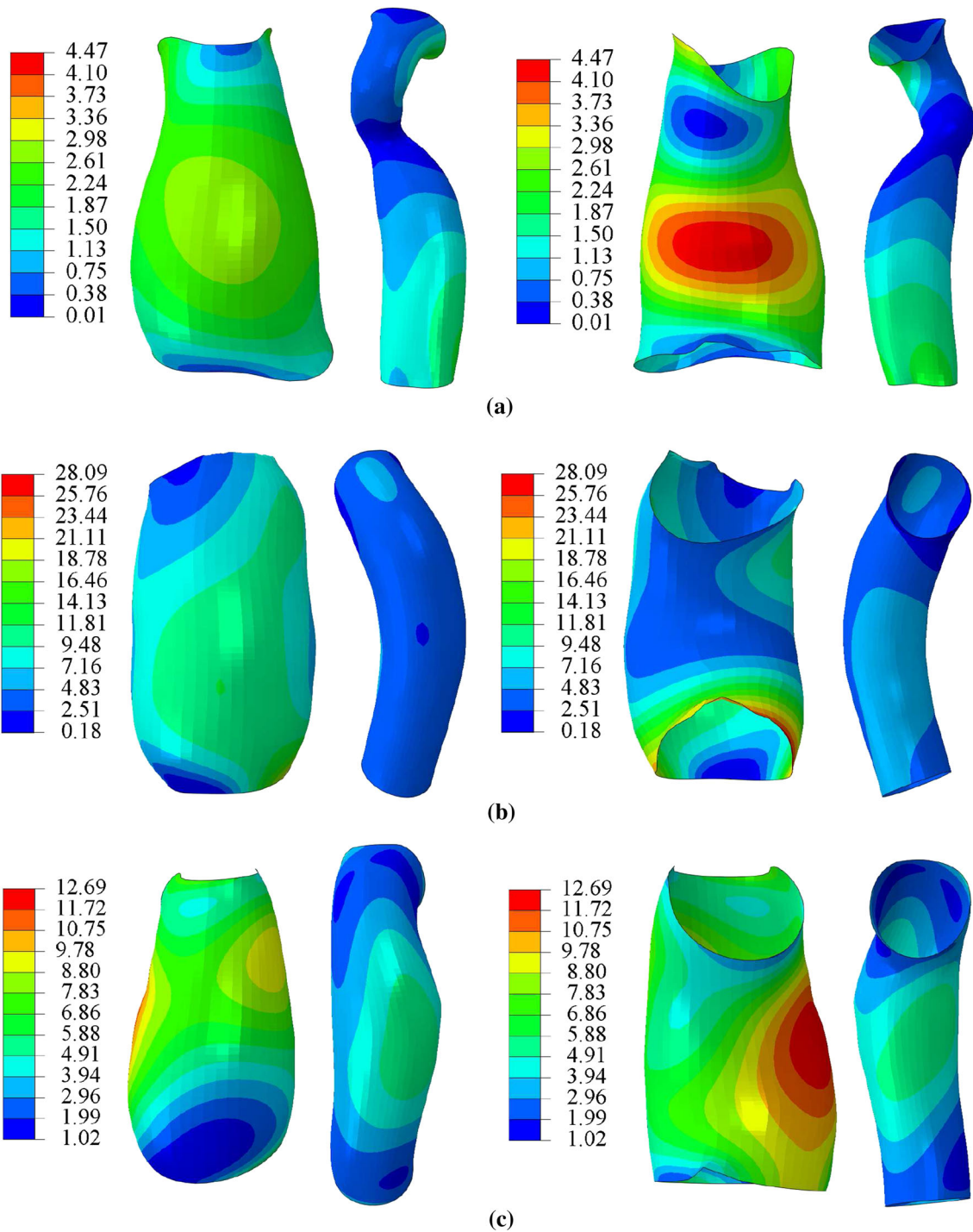


**Fig. 8** Distribution of local extensional stiffness (MPa mm) in ascending and descending aortas for Patient 1 (a), Patient 2 (b) and Patient 3 (c). Left and right show frontal and distal views respectively

## 4 Discussion

In this paper we have introduced an original method to reconstruct the stiffness distribution of the thoracic aorta from gated CT images considering ten phases of a cardiac cycle. This methodology requires tracking the deformations

of the aortic wall throughout a cardiac cycle from the gated CT images. The deformations were tracked without any additional information or marker indicating heterogeneous deformation in between the bifurcations.

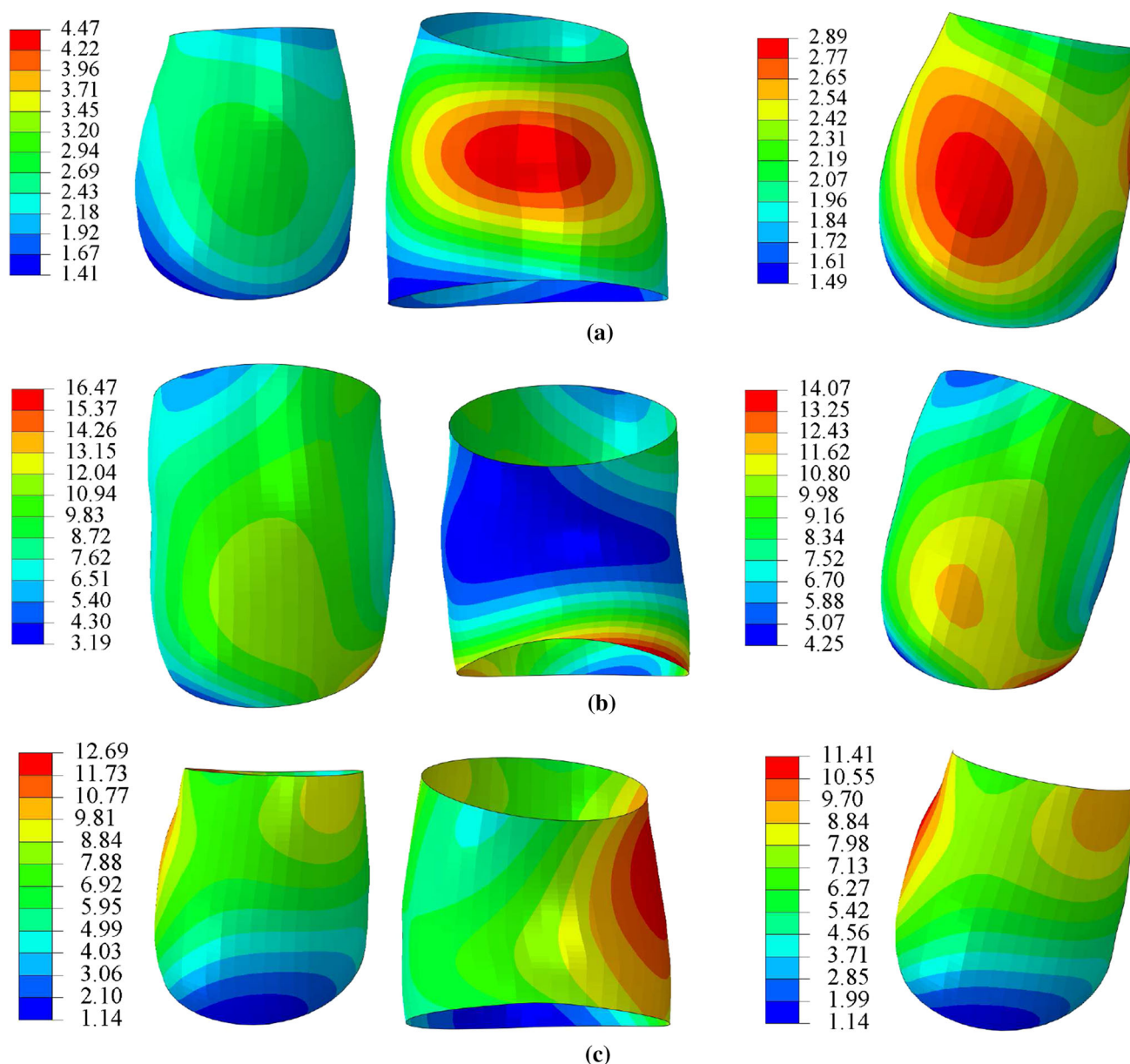


**Fig. 9** Distributions of local extensional stiffness (MPa mm) for Patient 1 (a), Patient 2 (b) and Patient 3 (c). Results in the left show frontal and distal views of in vivo. Results in the right demonstrate in vitro cut

#### 4.1 General remarks

For the first time ever, regional variations of stiffness properties across ATAA were reconstructed on 3 patients noninvasively. To achieve this reconstruction, a novel noninvasive inverse method was developed based on preoperative gated CT scans. The noninvasive identification of elastic properties of ATAA is highly important as our research group (Duprey et al. 2016; Trabelsi et al. 2017) recently showed that the extensional stiffness is significantly correlated with the stretch-based rupture risk of ATAA. Therefore, it is sig-

nificantly interesting to obtain the local extensional stiffness of the ascending thoracic aorta to detect pathological regions with the highest risks of rupture. Interestingly, our results indicate that the local extensional stiffness is higher in the aneurysmal ascending thoracic aorta than in the descending aorta and that the values are relatively higher than stiffness properties reported for healthy aortas. However, despite this general trend, the distribution of extensional stiffness is heterogeneous in the aneurysmal region, with large stiffness in the bulging part of aneurysm. The local loss of elasticity can be related to a more pronounced local remod-

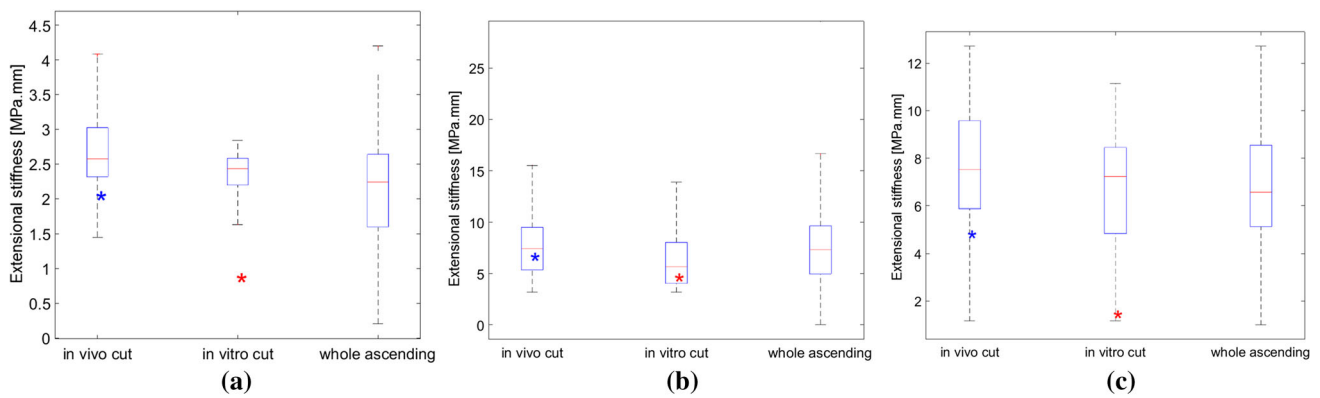


**Fig. 10** Median and interquartile range of the local extensile stiffness (MPa mm) obtained for in vivo cut, in vitro cut and whole ascending for Patient 1 (a), Patient 2 (b) and Patient 3 (c). The blue and the red

stars demonstrate the values of in vivo and in vitro cuts, respectively, which are calculated by Trabelsi et al. (2017) and Duprey et al. (2016)

eling with, for instance, a larger fraction of collagen fibers. Sassani et al. (2015) showed a large distribution of fiber orientations spanning from circumferential to longitudinal directions, which was also supported by Sokolis et al. (2012) stating that ATAA had no effect on strength. However, this can cause stiffening and extensibility reduction, corroborated with histological observation of elastin degradation but not collagen content. It could be interesting also to check the possible correlation of these regions with local concentration of wall shear stress induced by the blood flow (Malvindi et al. 2016). All these possible correlations between regional variations of extensile stiffness and local tissue composition or local hemodynamics effects are currently under study in our group on a cohort of patients. Over the past decades the biomechanical properties of the aorta have been widely investigated (Choudhury et al. 2009; Vorp et al. 2003; Geest et al. 2004; Okamoto et al. 2002; Fung 1993; Duprey et al. 2010; Holzapfel 2006; Mohan and Melvin 1982; Prendergast et al. 2003; Sokolis 2007). As the aortic tissues are intrinsically anisotropic, the identified stiffness provided by our method combines effects of the axial and circumferential extensile linearized stiffness. However, as we use only the pressure loading to solve the identification problem (we have no information on the axial tension in vivo), it is dominated by effects of the circumferential extensile linearized stiffness. This is in agreement with conclusions of Ferrara et al. (2016) who indicated that the weight of the circumferential elastic modulus is significantly higher than the weight of the longitudinal one in the aortic mechanical response to pressure variations. The maximum circumferential elastic modulus was reported in posterior region. Moreover, their results indicate that regardless of age and gender, the mean elastic modulus is larger in the circumferential direction. However, aging reduces the mean elastic modulus, and male has higher mean elastic modulus in comparison with female. Iliopoulos et al. (2009) support these results and state that cir-

cumferential specimens were stiffer than longitudinal ones in the posterior, left lateral, and all regions at physiologic and high stresses but not at low stresses. Furthermore, in agreement with Ferrara et al. (2016), they found no significant regional variations of aortic stiffness in the circumferential direction, and similarly at low stresses for longitudinal specimens, while at physiologic and high stresses the right lateral was the stiffest ATAA region. In the other study by the same group (Iliopoulos et al. 2008) it was shown that peak elastic modulus in the anterior region was significantly lower than that in the right, but not the left, lateral and posterior regions. Choudhury et al. (2009) studied local mechanical properties of healthy and diseased, bicuspid and tricuspid aortic valves (BAV and TAV), human ascending aorta. Indicating that BAV tissue was the thinnest and contained the largest fraction of collagen, they found significantly less elastin both in TAV and BAV tissue in contrast to healthy tissue, while on average the smallest stiffness was observed in TAV patients. The elastic modulus was not dependent on direction (isotropic) but it was dependent on the quadrant and tissue type. The medial quadrant was the most compliant and the lateral quadrant tissue was the stiffest.

Although most of these previous investigators carried out experimental tests on tissue samples excised from patients during surgery, or on cadavers, the material properties of tissues are commonly characterized averagedly across these samples and in conditions which may be far from in vivo conditions, such as for instance tensile test. Only recently, the use of digital image correlation (DIC) has made it possible to investigate the local material properties of excised aortic samples (Avril et al. 2010; Davis et al. 2015, 2016). Inverse methods were developed to process DIC measurements and reconstruct the regional variations of material properties, as for instance using a tension inflation tests keeping the cylindrical shape of the aorta (Bersi et al. 2016). Regional variations of constitutive properties make sense as

they can be related to local tissue adaptation through growth and remodeling (Humphrey 2008).

When excised aortic samples are tested *in vitro*, the results usually take the form of constitutive parameters in a strain energy density function (Holzapfel et al. 2000b). Strain energy density functions usually have a large number of constitutive parameters with possible couplings between each other and it was recently suggested to evaluate more functional parameters, such as for instance the linearized *in vivo* stiffness (Bersi et al. 2016). Here, we focused only on this linearized *in vivo* stiffness as we had only a noninvasive loading of the aorta across a limited range of strains through the variations of blood pressure. The noninvasive identification of the aortic stiffness was previously achieved averagedly across aortic segments either by measuring the aortic distensibility (Trabelsi et al. 2017) or by measuring the pulse wave velocity (Groenink et al. 1998), and relating these quantities to the aortic stiffness. Local non invasive identification was previously achieved using 4D ultrasound on the abdominal aorta (Joldes et al. 2016; Wittek et al. 2013) but the present study is the first one using gated CT scans and applying the approach onto the ascending thoracic aorta. The availability of these images allowed us to model subject-specific arterial configurations. Since a correlation between the stretch-based rupture risk and the tangent elastic modulus was found by Duprey et al. (2016), the methodology proposed here has potential to identify the rupture risk of aorta according to calculated local extensional stiffness.

It is important to point out the benefit of using a Fourier analysis (as done here for the regional reconstruction) instead of using simply diastolic and systolic geometries of the aorta (as done for distensibility measurements). Indeed, the distensibility is usually assessed by measuring the change of cross-sectional area of the aorta between diastole and systole, diastole being defined as the stage with minimum cross-sectional area and systole being defined as the stage with maximum cross-sectional area. There is always a significant uncertainty on the times at which the 10 phases of CT scans are acquired. If we could reduce this uncertainty and provided that a pressure curve can be measured simultaneously, the method could be easily extended to derive time variations of the stiffness throughout the whole cardiac cycle. However, we noticed that locally, the maximum deflection of the aorta, and its maximum strains, are not reached at the same stage of the cardiac cycle depending on the position (Fig. 1). It means that the response of the aorta to the pressure variations presents phase shifts depending on the position. These phase shifts are potentially the result of viscous effect but also of the combined action of the blood pressure and of the cardiac motion, which are not synchronized, as this was previously shown by Wittek et al. (2016). Due to these local phase shifts, it happens that the maximum strain of the aorta is not reached at systole for all the positions

and the minimum strain of the aorta is not reached at diastole. Therefore, taking the average change of strain between diastole and systole to derive the aortic stiffness, as done in the distensibility method (Duprey et al. 2016; Trabelsi et al. 2017), automatically underestimates the actual strain variations occurring throughout a cardiac cycle. The consequence of this strain underestimation should be a stiffness overestimation for the distensibility method. However, in this work, it can be compensated by another effect which we would like to point out here as well. Commonly, pressure variations are linearly related to stress variations without considering the effects of radius variations as we did in Eq. 16. However, we found that the term considering the effects of radius variations, namely  $\frac{\tau_1^0(\Delta r_1)}{(r_1^0)^2} - \frac{\tau_2^0(\Delta r_2)}{(r_2^0)^2}$ , is averagely responsible for about 10% of  $\Delta P$ , with local effects possibly reaching 50%. Neglecting this term, as it is traditionally done in distensibility assessment, induces an underestimation of stress variations. Combined with the strain underestimation explained previously, the stress underestimation results in a good agreement of the distensibility method with our novel inverse method. Nevertheless, future stiffness identifications should take into account all these effects as done in the current study.

## 4.2 Limitations

There are several limitations in this work which can be discussed as below:

- The inverse approach is based on local equilibrium equations similar to the ones derived in Bersi et al. (2016). These equations are obtained based on the principle of virtual work. It is worth noting that they are equivalent to the generalized Laplace's law which writes the local equilibrium between pressures and tensions in a membrane. Accordingly, it means that it is assumed that the aortic wall behaves as a membrane with no bending moments or no through thickness shear. Regions near the branches may not satisfy the membrane assumption, and were removed from the analysis.
- The present study used gated CT scans as a source of dynamic images of the aortic wall during the cardiac cycle. The use of X-ray may present a limitation for an extensive use of the methodology, especially if one wants to repeat the identification of aortic stiffness at different ages of ATAA growth, which would induce repeated irradiation for the patient. We are currently working on an extension of the method to images acquired with 4D MRI.
- The wall is assumed as a linearly elastic material within the systolic–diastolic range and we disregarded the layer-

specific wall properties and residual stresses existing in the ATAA wall.

- We here assumed an isotropic behavior of the arterial wall. It was not possible to consider anisotropic effects as only one type of loading was available: variations of the blood pressure. The characterization of anisotropic materials requires loading samples in different directions. The consequence of the isotropy assumption in our approach is that the identified extensional stiffness is a combination of the axial and circumferential stiffness, which may be different. However, the local curvatures being involved in Eq. 17, most of the weight is put on circumferential effects (the circumferential radius of curvature being significantly lower than the axial one), meaning that the identified extensional stiffness would be closer to the circumferential stiffness than to the axial stiffness if there was a significant difference between both.
- Average tensions existing in the aorta due to the action of the average blood pressure are also involved in Eq. 17. This comes from geometrical nonlinearity involved in finite deformations (Baek et al. 2007). These tensions were approximated using the approach of Joldes et al. (2016). This approach consists in achieving a linear elastic stress analysis on the same structure as the aorta, assigning a very large elastic modulus. The approach is valid for membrane structures. The membrane assumption was previously shown to be a good approximation for elastostatics of aortic aneurysms (Lu et al. 2007).
- Due to the removal of in vivo loadings, the artery experiences an elastic recoiling. Even when these loadings are removed, internal or residual stresses still exist in the tissues. An effect of these internal stresses can be observed in arteries with the well-known opening angle (Mousavi and Avril 2017). Moreover, Sokolis (2015) have provided evidence of residual stresses in both the circumferential and longitudinal directions considering different wall layers of ATAA. Therefore, disregarding the presence of residual stresses and considering the arterial wall as a 3D membrane with uniform thickness can be considered as additional limitations of the current work. Nevertheless, despite these limitations, the extensional stiffness provided by our methodology is still a useful indicator of local tissue altered remodeling.
- The segmented geometries have some local irregularities (bumps) due to image noise at each phase of the cardiac cycle. The spatial frequency of these irregularities is high and their effect is filtered out by Fourier polynomial smoothing. However, if one wanted to obtain spatial variations of material properties with a higher spatial res-

olution, one would have to address the issue of these geometric irregularities.

## 5 Conclusion

Regional variations of stiffness properties across ATAA were reconstructed on 3 patients noninvasively. To achieve this reconstruction, a novel noninvasive inverse method was developed based on preoperative gated CT scans. The noninvasive identification of elastic properties of ATAA is highly important as our research group Duprey et al. (2016) and Trabelsi et al. (2017) recently showed that the extensional stiffness is significantly correlated with stretch-based rupture risk of ATAA. It would be interesting in future studies to consider a cohort with a larger number of patients in order to interpret regional variations of stiffness properties in ATAAs in terms of local hemodynamics effects and of local tissue remodeling.

**Acknowledgements** The authors are grateful to the European Research Council for Grant ERC-2014-CoG BIOLOCHANICS.

## Compliance with ethical standards

**Conflict of interest** The authors declare that they have no conflict of interest.

## References

- Antiga L, Steinman DA (2004) Robust and objective decomposition and mapping of bifurcating vessels. *IEEE Trans Med Imaging* 23(6):704–13
- Avril S, Badel P, Duprey A (2010) Anisotropic and hyperelastic identification of in vitro human arteries from full-field optical measurements. *J Biomech* 43:2978–85
- Baek S, Gleason RL, Rajagopal KR, Humphrey JD (2007) Theory of small on large: potential utility in computations of fluid-solid interactions in arteries. *Comput Methods Appl Mech Eng* 196:3070–78
- Bersi MR, Belliniand C, Di Achille P, Humphrey JD, Genovese K, Avril S (2016) Novel methodology for characterizing regional variations in the material properties of murine aortas. *J Biomech Eng* 138:071005
- Bickerstaff LK, Pairolero PC, Hollier LH, Melton LJ, Van Peenen HJ, Cherry KJ et al (1982) Thoracic aortic aneurysms: a population-based study. *Surgery* 92:1103–08
- Chau KH, Elefteriades JA (2013) Natural history of thoracic aortic aneurysms: size matters and plus moving beyond size. *Prog Cardiovasc Dis* 56(1):74–80
- Choudhury N, Olivier B, Leonie R, Dominique T, Raymond C, Jagdish B et al (2009) Local mechanical and structural properties of healthy and diseased human ascending aorta tissue. *Cardiovasc Pathol* 18:83–91
- Coady MA, Rizzo JA, Hammond GL, Kopf GS, Elefteriades JA (1999) Surgical intervention criteria for thoracic aortic aneurysms: a study

- of growth rates and complications. *Ann Thorac Surg* 67(6):1922–6
- Coady MA, Rizzo JA, Hammond GL, Mandapati D, Darr U, Kopf GS, Elefteriades JA (1997) What is the appropriate size criterion for resection of thoracic aortic aneurysms? *J Thorac Cardiovasc Surg* 113(3):476–91
- Davis FM, Luo Y, Avril S, Duprey Ambroise A, Lu J (2016) Local mechanical properties of human ascending thoracic aneurysms. *J Mech Behav Biomed Mater* 61:235–49
- Davis FM, Luo Y, Avril S, Duprey A, Lu J (2015) Pointwise characterization of the elastic properties of planar soft tissues: application to ascending thoracic aneurysms. *Biomech Model Mechanobiol* 14:967–78
- Duprey A, Khanafer K, Schlicht M, Avril S, Williams D, Berguer R (2010) In vitro characterisation of physiological and maximum elastic modulus of ascending thoracic aortic aneurysms using uniaxial tensile testing. *Eur J Vasc Endovasc Surg* 39(6):700–7
- Duprey A, Trabelsi O, Vola M, Favre JP, Avril S (2016) Biaxial rupture properties of ascending thoracic aortic aneurysms. *Acta Biomater* 42:273–85
- McGlothin T (ed) (2011) *Biomechanics and mechanobiology of aneurysms*. Springer, Heidelberg
- Elefteriades JA, Farkas EA (2010) Thoracic aortic aneurysm clinically pertinent controversies and uncertainties. *J Am Coll Cardiol* 55(9):841–57
- Ferrara A, Morganti S, Totaro P, Mazzola A, Auricchio F (2016) Human dilated ascending aorta: mechanical characterization via uniaxial tensile tests. *J Mech Behav Biomed Mater* 53:257–71
- Fillinger MF, Marra SP, Raghavan ML, Kennedy FE (2003) Prediction of rupture risk in abdominal aortic aneurysm during observation: wall stress versus diameter. *J Vasc Surg* 37(4):724–32
- Fung YC (1993) *Biomechanics: mechanical properties of living tissues*. Springer, Berlin
- García-Herrera CM, Atienza JM, Rojo FJ, Claes E, Guinea GV, Celentano DJ, García-Montero C, Burgos RL (2008) Mechanical behaviour and rupture of normal and pathological human ascending aortic wall. *Med Biol Eng Comput* 50(6):559–66
- Geest JP Vande, Di Martino ES, Bohra A, Makaroun MS, Vorp DA (1085) A biomechanics-based rupture potential index for abdominal aortic aneurysm risk assessment: demonstrative application. *Ann N Y Acad Sci* 11–21:2006
- Geest JP Vande, Sacks MS, Vorp DA (2004) Age dependency of the biaxial biomechanical behavior of human abdominal aorta. *J Biomech Eng* 126:815–22
- Groenink M, de Roos A, Mulder BJ, Spaan JA, van der Wall EE (1998) Changes in aortic distensibility and pulse wave velocity assessed with magnetic resonance imaging following beta-blocker therapy in the marfan syndrome. *Am J Cardiol* 82:203–8
- Haker S, Angenent S, Tannenbaum A, Kikinis R (2000) Nondistorting flattening maps and the 3-D visualization of colon CT images. *IEEE Trans Med Imaging* 19:665–670
- Hibbitt, Karlsson & Sorensen (2011) *Abaqus-Theory manual*, 6.11-3 edn. Hibbitt, Karlsson & Sorensen, Providence
- Holzappel GA (2006) Determination of material models for arterial walls from uniaxial extension tests and histological structure. *J Theor Biol* 238:290–302
- Holzappel GA, Gasser TC, Ogden RW (2000) A new constitutive framework for arterial wall mechanics and a comparative study of material models. *J Elast Phys Sci Solids* 61(1):1–48
- Holzappel GA, Gasser TC, Ogden RW (2000) A new constitutive framework for arterial wall mechanics and a comparative study of material models. *J Elast Phys Sci Solids* 61(1–3):1–48
- Humphrey JD (2008) Vascular adaptation and mechanical homeostasis at tissue, cellular, and sub-cellular levels. *Cell Biochem Biophys* 50:53–78
- Iliopoulos DC, Deveja RP, Kritharis EP, Perrea D, Sionis GD, Toutouzias K, Stefanadis C, Sokolis DP (2008) Regional and directional variations in the mechanical properties of ascending thoracic aortic aneurysms. *Med Eng Phys* 31(1):1–9
- Iliopoulos DC, Kritharis EP, Giagini AT, Sokolis DP, Papadodima SA (2009) Ascending thoracic aortic aneurysms are associated with compositional remodeling and vessel stiffening but not weakening in age-matched subjects. *J Thorac Cardiovasc Surg* 137(1):101–9
- Johansson G, Markström U, Swedenborg J (1995) Ruptured thoracic aortic aneurysms: a study of incidence and mortality rates. *J Vasc Surg* 21(6):985–8
- Joldes GR, Miller K, Wittek A, Doyle B (2016) A simple, effective and clinically applicable method to compute abdominal aortic aneurysm wall stress. *J Mech Behav Biomed Mater* 58:139–48
- Lu J, Zhou X, Raghavan ML (2007) Inverse elastostatic stress analysis in pre-deformed biological structures: demonstration using abdominal aortic aneurysms. *J Biomech* 40:693–6
- Malvindi PG, Pasta S, Raffa GM, Livesey S (2016) Computational fluid dynamics of the ascending aorta before the onset of type a aortic dissection. *Eur J Cardio-Thorac Surg* 51(3):597–99
- Martin C, Sun W, Pham T, Elefteriades J (2013) Predictive biomechanical analysis of ascending aortic aneurysm rupture potential. *Acta Biomater* 9(12):9392–400
- Martufi G, Gasser TC, Appoo JJ, Di Martino ES (2014) Mechanobiology in the thoracic aortic aneurysm: a review and case study. *Biomech Model Mechanobiol* 13:917–928
- Mohan D, Melvin JW (1982) Failure properties of passive human aortic tissue. I—uniaxial tension tests. *J Biomech* 15:887–902
- Mousavi SJ, Avril S (2017) Patient-specific stress analyses in the ascending thoracic aorta using a finite-element implementation of the constrained mixture theory. *Biomech Model Mechanobiol* 16(5):1765–77
- Mousavi SJ, Farzaneh S, Avril S (2017) Computational predictions of damage propagation preceding dissection of ascending thoracic aortic aneurysms. *Int J Numer Method Biomed Eng* 34(4):e2944
- Okamoto RJ, Wagenseil JE, DeLong WR, Peterson SJ, Kouchoukos NT, Sundt TM 3rd (2002) Mechanical properties of dilated human ascending aorta. *Ann Biomed Eng* 30:624–35
- Prendergast PJ, Lally C, Daly S, Reid AJ, Lee TC, Quinn D et al (2003) Analysis of prolapse in cardiovascular stents: a constitutive equation for vascular tissue and finite-element modelling. *J Biomech Eng* 125:692–99
- Ramanath VS, Oh JK, Sundt TM 3rd, Eagle KA (2009) Acute aortic syndromes and thoracic aortic aneurysm. *Mayo Clin Proc* 84(5):465–81
- Sassani SG, Tsangaris S, Sokolis DP (2015) Layer- and region-specific material characterization of ascending thoracic aortic aneurysms by microstructure-based models. *J Biomech* 48(14):3757–65
- Sokolis DP (2007) Passive mechanical properties and structure of the aorta: segmental analysis. *Acta Physiol (Oxf)* 190:277–289
- Sokolis DP (2015) Effects of aneurysm on the directional, regional, and layer distribution of residual strains in ascending thoracic aorta. *J Mech Behav Biomed Mater* 46:229–43
- Sokolis DP, Kritharis EP, Giagini AT, Lampropoulos KM, Papadodima SA, Iliopoulos DC (2012) Biomechanical response of ascending thoracic aortic aneurysms: association with structural remodelling. *Comput Methods Biomech Biomed Eng* 15(3):231–48
- Trabelsi O, Davis FM, Rodriguez-Matas JF, Duprey A, Avril S (2015) Patient specific stress and rupture analysis of ascending thoracic aneurysms. *J Biomech* 48(10):1836–43
- Trabelsi O, Gutierrez M, Farzaneh S, Duprey A, Avril S (2017) A non-invasive technique for ATAA rupture risk estimation. *J Biomech*. <https://doi.org/10.1016/j.jbiomech.2017.11.012>
- van Disseldorp EM, Petterson NJ, Rutten MC, van de Vosse FN, van Sambeek MR, Lopata RG (2016) Patient specific wall stress analy-

- sis and mechanical characterization of abdominal aortic aneurysms using 4D ultrasound. *Eur J Vasc Endovasc Surg* 52:635-42
- Vorp DA, Schiro BJ, Ehrlich MP, Juvonen TS, Ergin MA, Griffith BP (2003) Effect of aneurysm on the tensile strength and biomechanical behavior of the ascending thoracic aorta. *Ann Thorac Surg* 75:1210-14
- Wittek A, Karatolios K, Bihari P, Schmitz-Rixen T, Moosdorf R, Vogt S, Blase C (2013) In vivo determination of elastic properties of the human aorta based on 4D ultrasound data. *J Mech Behav Biomed Mater* 27:167-183
- Wittek A, Karatolios K, Fritzen CP, Bereiter-Hahn J, Schieffer B, Moosdorf R, Vogt S, Blase C (2016) Cyclic three-dimensional wall motion of the human ascending and abdominal aorta characterized by time-resolved three-dimensional ultrasound speckle tracking. *Biomech Model Mechanobiol* 15(5):1375-88

**Publisher's Note** Springer Nature remains neutral with regard to jurisdictional claims in published maps and institutional affiliations.